

# **Friction stir gradient alloying: a high-throughput method to explore the influence of V in enabling HCP to BCC transformation in a $\gamma$ -FCC dominated high entropy alloy**

Priyanka Agrawal<sup>a,b</sup>, Shivakant Shukla<sup>a,\$</sup>, Sanya Gupta<sup>a</sup>, Priyanshi Agrawal<sup>a,b</sup>, Rajiv S. Mishra<sup>a,b,\*</sup>

<sup>a</sup>Center for Friction Stir Processing, Department of Materials Science and Engineering, University of North Texas, Denton, TX 76207 USA

<sup>b</sup>Advanced Materials and Manufacturing Processes Institute, University of North Texas, Denton, TX 76207, USA

\*Corresponding author: [Rajiv.Mishra@unt.edu](mailto:Rajiv.Mishra@unt.edu)

\$Current address: Oak Ridge National Laboratory, Oak Ridge, TN 37830, USA

## **Abstract**

The compositional possibilities in high entropy alloys (HEAs) is very vast and effective strategies are needed for establish potential alloy chemistries. In this study, friction stir gradient alloying (FSGA), a recently-introduced high-throughput (HT) technique incorporating compositional and microstructural gradients, was used to explore the possibility of introducing a bcc transformation domain in  $\gamma$ -fcc dominated TRIP HEA  $\text{Fe}_{38.5}\text{Mn}_{20}\text{Cr}_{15}\text{Co}_{20}\text{Si}_5\text{Cu}_{1.5}$  (at.%) by vanadium addition. FSGA has accelerated the process of attaining the composition-microstructure library and the results suggest that vanadium addition of ~1 at.% results in nucleation of  $\alpha$ -bcc. This is the first observation of  $\varepsilon$ -hcp to  $\alpha$ -bcc transformation in a TRIP HEA and supports the Olson-Cohen model of martensitic transformation ( $\gamma$ -fcc  $\rightarrow$   $\varepsilon$ -hcp  $\rightarrow$   $\alpha$ -bcc).  $\varepsilon$ -hcp is nucleated with a pyramidal orientation by the formation of planar faults on the {111} close-packed planes of  $\gamma$ -fcc, and  $\alpha$ -bcc is nucleated in the vicinity of  $\varepsilon$ -hcp along the {111}  $\gamma$ -fcc trace. There are indications for the

formation of basal orientated  $\varepsilon$ -hcp from intersecting  $\varepsilon$ -hcp planes orientated for the pyramidal slip. Thus, the study shows the nucleation and growth of the  $\alpha$ -bcc phase attributed to the dual effects of chemistry and strain and potential co-existence of all the three phases.

**Keywords:** *friction stir gradient alloying; transforming high entropy alloys; vanadium alloying; hcp-bcc transformation*

## 1. Introduction

High entropy alloys (HEAs) have established a new paradigm for alloy exploration[1–6]. HEAs are known to give good strength and ductility, a combination that pushes the boundaries of what is possible in conventional metallic systems[7,8]. Most of these studies have focused mainly on exploring equiatomic or near equiatomic systems that result in a single FCC phase[9,10]. At present, the research focus of high entropy alloys is muti-phase non-equimolar ratio components [11,12]. HEAs are being designed progressively to have a low stacking fault energy (SFE) that leads to significant improvement in work hardening rate via transformation and/or twinning-induced plasticity (TRIP and/or TWIP). In the last few years, systems have been explored to take advantage of the TRIP effect that results in dual-phase strengthening with FCC and HCP phases[13].

Apart from FCC-HCP, FCC-BCC transformations are well-established in general (Olson-Cohen model[14–16]) and are being explored in HEAs[15,17]. Exploring and understanding the different combinations of FCC-HCP-BCC transformations for HEAs is fundamentally appealing. Recently Mishra and co-workers[18–25] have focused on engineering metastability in the TRIP HEA domain systems. These studies have been carried out to cover the transformation domain by different combinations of alloy chemistry and thermo-mechanical processes[18–25].

The vast compositional space of HEAs creates an enormous challenge to identify compositions of interest and becomes even more complicated in the case of metastable TRIP HEAs. To overcome this challenge, experimentally, a recently developed high throughput (HT) technique, friction stir gradient alloying (FSGA), was proposed by Shukla et al.[26]. The technique consists of putting a slice of alloying element in the groove of a base HEA. Subsequent friction stir processing (FSP), which is a high temperature severe plastic deformation technique, of the assembly results in a gradual increase in alloying content of the additional element. In the present example of TRIP HEA, compositional variation in alloy composition not only impacts the phase fraction in the as-processed condition, but also affects the deformation induced transformation. In addition to the gradient in chemistry, FSP creates variation in processing strain[27], from high strain at the advancing side to low strain on the retreating side of the FSGA run. This variation in strain affects the grain size and phase fraction due to the TRIP effect. Hence, these variants provide an excellent opportunity *to create composition-microstructure library for the screening of metastability-assisted HEAs*. Additionally for a given composition, gradient microstructure is reported to have improved strength and ductility as compared to a uniform one[28–30]. Furthermore, friction stir-based technique enjoys several benefits over other HT techniques. As compared to additive manufacturing, FSGA produces a wrought microstructure, which is an important consideration for alloy performance[31]. FSGA allows one to carry out the microstructural study of deformed samples which is difficult in HT techniques like vapor deposition where only a library of chemistry and phases can be obtained without any ability to evaluate thermo-mechanical processing aspects or mechanical behavior studies[32].

Nene et al.[33,34] studied the effect of chemistry by adding just 1.5 at. % Cu in the  $\epsilon$ -hcp dominant  $\text{Fe}_{40}\text{Mn}_{20}\text{Cr}_{15}\text{Co}_{20}\text{Si}_5$  (CS-HEA), with a complete change in phase stability to a stabilized  $\gamma$ -fcc

phase. The resultant HEA  $\text{Fe}_{38.5}\text{Mn}_{20}\text{Cr}_{15}\text{Co}_{20}\text{Si}_5\text{Cu}_{1.5}$ , denoted as Cu-HEA, possesses exceptional properties that include excellent strength, ductility, fatigue, and corrosion resistance[34,35]. In this regard, recently Shukla et al.[26] studied the effect of gradient variation of Cu on the phase stability and mechanical property of the CS-HEA. The starting/base material was  $\epsilon$ -hcp dominant CS-HEA, which by the addition of Cu shifted towards a mixture of  $\epsilon$ -hcp +  $\gamma$ -fcc phase. Apart from phase fraction, grain size refinement was also observed with an increase in Cu content.

HEAs are designed on core effects such as lattice distortion, cocktail effect, sluggish diffusion, and high entropy of mixing[36,37]. Vanadium is reported to improve the mechanical properties of the HEAs, mainly the strength due to its large atomic size leading to lattice distortions. Yeh et al.[38–40] were among the early researchers to study the effect of vanadium in HEAs resulting in  $\alpha$ -bcc and/or  $\sigma$ -bct phases that led to an improvement in compressive strength, hardness and wear resistance. Subsequent studies confirmed that the increase in strength, which was due to lattice distortion, resulted in high misfit, followed by obstacles for dislocation movement and thus effective slip resistance[17,41–43]. Barron et al.[44] presented V as a promising candidate in the ternary and quaternary HEAs, V-Cr-Mn, and V-Cr-Mn-Ti, for nuclear fusion applications.

Given that the addition of V leads to nucleation of  $\alpha$ -bcc and/or  $\sigma$ -bct phase, FSGA of V was carried out on  $\gamma$ -fcc dominant Cu-HEA. This information will provide guidance in picking the critical V composition from the library of compositions and microstructures created via FSGA, for the nucleation of  $\alpha$ -bcc.

## 2. Methods

A metastable Cu-HEA ( $\text{Fe}_{38.5}\text{Mn}_{20}\text{Cr}_{15}\text{Co}_{20}\text{Si}_5\text{Cu}_{1.5}$ ) (composition in at%) [45] was used as the base material with plate thickness of ~10 mm.

For gradient alloying, three pure V (99.99% purity) strips were prepared via electric discharge machining (EDM) with dimensions 3 mm height, 25.4 mm length, and thickness 0.5 mm. The V strips were polished to remove the oxide layer from EDM cutting to final widths of 0.1, 0.2, and 0.3 mm. The base metal slab was milled for three channels using CNC milling of ~3 mm height, length 25.4 mm, and different widths (0.1, 0.2, and 0.3 mm). Dimensions of the channels and V strips were controlled carefully so they fit perfectly for the FSGA process. Friction stir processing of the assembly was carried out in air using W-25%Re tool with shoulder diameter, root diameter, pin diameter, and pin height 12 mm, 7.5 mm, 6 mm, and 3.7 mm, respectively. The parameters used during FSGA are listed in Table 1.

Table 1: Friction stir gradient alloying (FSGA) parameters for pure V addition in Cu-HEA.

Alloying material	V (99.99% purity)
Tool	W-25%Re
Rotation speed (rotation per minute) (RPM)	450
Transverse speed (inch per minute) (ipm)	1.0
Tilt angle (°)	-1.5

Mini tensile samples were milled using EDM from the processed block with different vanadium content with ~5 mm gauge length, ~1.2 mm thickness, and ~1.25 mm gauge. The samples were machined such that the first sample is from the processed block without the V strip and is used as a control point sample to study and compare the properties of samples with different V content. As the mini-tensile samples were also aimed for microscopy, the samples were ground with emery papers with final grit size as 4000 and later polished till 0.02  $\mu\text{m}$  colloidal silica suspension for a mirror finish.

The samples were imaged for microstructure and composition using scanning electron microscopy (SEM), whereas the phase and texture were investigated via X-ray diffraction (XRD) and SEM electron backscattered diffraction (EBSD). Transmission electron microscopy (TEM) was carried out for specific samples to confirm the results. The XRD experiments were focused on obtaining the bulk texture using a Rigaku Ultima III X-ray machine, with Cu K<sub>α</sub> radiation operated at 40 kV and 44 mA with a 2θ scan range of 40–100 degrees and a scan speed of 1 degree per minute. SEM imaging was done on FEI Nova NanoSEM 230 in BSE mode equipped with an EDAX Octane Elite detector for compositional mapping. The NanoSEM is also equipped with a Hikari Super EBSD that was used for micro texture experiments and TSL OIM8 software for analysis. For TEM, the samples were milled out with FEI Nova 200 NanoLab Dual Beam Focused Ion Beam (FIB)/Field Emission Scanning Electron Microscope (FE-SEM) with platinum gun injection system (Pt GIS). TEM microscopy was carried out on FEI Tecnai G2 F20 S-Twin 200keV FE-STEM. Precession electron diffraction (PED), TEM based OIM was carried out to obtain the phase fraction along with orientation information. TOPSPIN software was used for the acquisition of the PED data with ASTAR hardware, both from NanoMEGAS.

### 3. Results and Discussion

#### 3.1 *Macro texture studies*

The process of FSGA, shown as a schematic in Figure 1, resulted in a processed block with different V content in the weld direction. Four mini-tensile samples were milled out for testing and microscopy: A, B, C, and D from near the lower V end as shown in Figure 2 (a). Note that the tensile specimen will have gradient of composition and microstructure. So, the results should not be interpreted in the regular manner. The intention here is to get first results of local composition-microstructure-phase transformation information. The milling of samples from the higher V end

was avoided due to processing defects. Figure 2 (b) presents XRD analysis from the polished samples with different V content showing the evolution of  $\alpha$ -bcc peaks along with  $\gamma$ -fcc and  $\varepsilon$ -hcp peaks. Sample A is the FSP sample without any V; the control sample, with  $\gamma$ -fcc as the dominant phase and  $\varepsilon$ -hcp as the minor phase. The XRD peaks for sample A confirm the presence of  $\gamma$ -fcc and  $\varepsilon$ -hcp phases. With the addition of V, samples B, C, and D show diffraction extra peaks at  $\sim 82^\circ$  degrees that correspond to  $\alpha$ -bcc  $\{211\}$  set of planes. A minor peak (around  $38^\circ$ ) corresponds to  $\{110\}$  set of planes for  $\alpha$ -bcc. For V-containing samples, the extra  $\varepsilon$ -hcp peak corresponds to  $\{102\}$  set of planes at  $\sim 64^\circ$ ; while the intensity of  $\{220\}$  and  $\{311\}$  peaks corresponding to  $\gamma$ -fcc and  $\gamma$ -fcc+ $\varepsilon$ -hcp increases with the increase in V content. This confirms that the  $\alpha$ -bcc and  $\varepsilon$ -hcp phase fractions evolve with V content.

### ***3.2 Microstructural studies to establish the phases present***

SEM on all samples enabled further microstructural analysis to obtain micro-images, compositional maps, phase maps, and texture maps. Figure 3 presents the SEM-backscattered electron (BSE) images of the processed samples with different V content. Phases with different contrast are observed: the matrix in grey contrast expected to be  $\gamma$ -fcc; and the other two phases with light and dark contrast, which will be addressed in the subsequent discussion. Figures 3 (a) and (b) are from the control sample A, without any V. Figure 3 (b) is a high magnification image from sample A where FSP leads to patches of the matrix in grey contrast with finer grains and phase with light contrast. Figures 3 (c) and (d) are for sample B with the lowest V content; Figures 3 (e) and (f) are for sample C, with medium V content; whereas Figures 3 (g) and (h) are for sample D, with the highest V. With the increase in V content the fraction of the dark phase increases, and is expected to be V-rich. This could be the reason why there is no phase with dark contrast in

micrographs from sample A (Figures 3 (a) and (b)). FSP with the parameters listed in Table 1 led to heterogeneous mixing (Figure 3). Localized regions with i) coarse and fine grains, ii) phases present, and iii) improper mixing of V as seen from patches of dark phases are all attributed to the inability of obtaining a homogeneous deformation. The higher atomic size of V than the matrix leads to lattice distortion, with a resultant increase in strength and a decrease in ductility of the alloy as reported in the literature[17,41–43]. This could explain the defects and heterogeneous mixing for the FSP run. An optimum FSP window is a combination of traverse and rotational rates but also depends on the tool with features used for proper material flow, which leads to homogenous deformation. Changing the parameters for homogeneous deformation and proper mixing of V lead to defect generation; hence, a parameter that does not create defects at the expense of homogenous mixing was chosen. There are studies reported to obtain heterogeneous microstructure in HEAs via FSP that lead to improved properties[46,47]. These outcomes offered the opportunity to study the evolution of phases with both chemistry and strain. To confirm the composition and phase of the contrasting features observed in SEM-BSE, further EDS and EBSD were carried out.

Detailed composition mapping was performed for higher V content samples C and D (Figure 4). Figure 4 (a) gives EDS results for sample C for a region with all three phases in different contrast in the SEM-BSE (Figure 3 (f) area bounded by green square). A localized region with high V (Figure 4 (a<sub>1</sub>)) corresponds to the dark patch in Figure 4 (a). Apart from that, the V composition map confirms the diffusion and mixing of V for the FSP parameters used. The region rich with V is lean with other elements (Figures 4 (a<sub>1</sub>-a<sub>7</sub>)). Figure 4 (b) is for sample D with the highest V, the same region as Figure 3 (h) (region bounded by the green square). Observations similar to sample C appear in sample D. Figure 4 (b<sub>1</sub>) is the V map of regions with different V content. Interestingly,

Cr composition maps (Figures 4 (a<sub>3</sub>) and 4 (b<sub>3</sub>)) not showing partitioning as compared to other elemental maps could be because Cr is next to V in the periodic table, with almost similar atomic radii. Also, like V, Cr is a bcc phase stabilizer in HEAs. Although the SEM-BSE images showed heterogeneous mixing, which still holds for EDS maps, the FSP parameters did result in V mixing and not just distribution of regions of pure unmixed V. Figure 4 (c) compares the quantitative elemental composition of samples C and D with the base Cu-HEA. Quantitative analysis along with the maps reiterates that V content has increased along with the diffused area along the weld direction.

Further EBSD was carried out to study phase fraction evolution with an increase in V and to correlate the SEM-BSE images and EDS maps to the individual phases. Phase maps from the EBSD study are presented in Figure 5 where the green phase corresponds to  $\gamma$ -fcc, red to  $\varepsilon$ -hcp and yellow to  $\alpha$ -bcc with V content. Figure 5 (a) is for sample A, processed base alloy without V, consisting of primarily the  $\gamma$ -fcc phase with around 2% of  $\varepsilon$ -hcp phase. With an increase in V content, the  $\alpha$ -bcc phase evolves in the vicinity of the  $\varepsilon$ -hcp (Figures 5 (b) to (d)). The deformation of systems with dominant  $\gamma$ -fcc phase and low SFE contributes to the formation of faults that lead to the  $\varepsilon$ -hcp embryos and is well-documented. Due to processing strain,  $\gamma$ -fcc transforms to  $\varepsilon$ -hcp phase as a result of the TRIP effect, thereby leading to a decrease in its phase fraction[34]. Figure 5 (e) gives the plot for phase fraction trends for all the samples where, with the increase in V content,  $\gamma$ -fcc is decreasing, while  $\varepsilon$ -hcp and  $\alpha$ -bcc phase fractions are increasing.

Figure 6 compares the SEM-BSE image (Figure 3 (h)), SEM-EDS map (Figure 4 (b<sub>1</sub>)), and SEM-EBSD phase map (Figure 5 (d)), which are all from sample D with the highest V and the *same* region. This exercise makes one to one correlation to identify the phases observed with different

contrast in SEM-BSE images to composition and crystal structure from EDS map and EBSD phase map, respectively. The dark phase from the BSE image is rich in V and is the  $\alpha$ -bcc phase. The  $\alpha$ -bcc phase is surrounded by the  $\varepsilon$ -hcp phase, which is light in contrast and with diffused V content. Further association shows the grey contrast to be the matrix  $\gamma$ -fcc with lean V content and with varying grain size due to heterogeneous deformation. The interesting feature common to all V content samples is that  $\alpha$ -bcc is observed in the vicinity of  $\varepsilon$ -hcp. This suggests that deformation induced transformation of from  $\varepsilon$ -hcp to  $\alpha$ -bcc may be possible.

### ***3.3 Mechanical testing***

After establishing the phases present, the samples were tested under tension to study the effect of strain on the nucleation of BCC. Note that as mentioned earlier, such tensile tests with gradient composition and microstructure are not ideal for strength and ductility data, but the data can be used for further guidance for specific alloy development. An advantage of FSGA, as opposed to HT techniques like vapor deposition[32], is that apart from composition-microstructure, limited mechanical behavior studies can be carried out as shown in Figure 7. Figure 7 (a) shows the engineering stress-strain curves at room temperature for all the samples tested under tension. It is observed that the strength increases with the V content (Figure 7 (b)). Since  $\alpha$ -bcc is a harder phase than the austenite matrix[48], the onset of the transformation is reported to contribute to additional work hardening. The full report on strength, ductility, and additional work hardening is expected when the alloy is synthesized with the right V composition for the system to show the full extent of transformation to  $\alpha$ -bcc.

### ***3.4 Strain-induced nucleation of $\alpha$ -bcc from $\varepsilon$ -hcp***

During FSGA, apart from the gradient in chemistry, the process leads to shear deformation gradient from advancing to retreating side[27]. Olson and Cohen[14] proposed a model for the fundamental understanding of hcp to bcc phase transformation. They predicted the strain-induced hcp transformation to bcc in steels, where transformation depended on the new sites being created during plastic deformation at the intersection of hcp  $(10\bar{1}0)$  planes. The idea was seeded by Bogers and Burgers on fcc to bcc transformation[49], where they studied combinations to obtain the intersecting  $\{111\}[112]$  shear systems of the parent  $\gamma$ -fcc phase that result in the nucleation of the daughter  $\alpha'$ -bcc phase due to shear displacements. Venables[50] observed the nucleation of  $\alpha'$  martensite (bcc) at the intersection of two  $\varepsilon$ -hcp plates in 304 austenitic stainless steel (fcc), during deformation at 78K where the Kurdjumov and Sachs[51] orientation relationship was observed:  $(111)_\gamma \parallel (0001)_\varepsilon \parallel (011)_\alpha$  and  $[10\bar{1}]_\gamma \parallel [11\bar{2}0]_\varepsilon \parallel [1\bar{1}1]_\alpha$ . The  $\varepsilon$ -hcp was observed to promote the nucleation site of  $\alpha'$ martensite (bcc/bct) due to shear deformation. As observed by Bogers and Burgers[49], there were other reports where  $\varepsilon$ -hcp was observed to be not a necessary condition for the nucleation of  $\alpha'$ martensite (bcc/bct). The  $\alpha'$ martensite (bcc/bct) could be nucleated from preferentially orientated  $\gamma$ -fcc to the tensile axis, suppressing the formation of  $\varepsilon$ -hcp. Thus the martensitic sequence was reported to be dependent on the SFE of the parent  $\gamma$ -fcc[52]. The sequence was reported to be  $\gamma$ -fcc  $\rightarrow$   $\varepsilon$ -hcp  $\rightarrow$   $\alpha'$ -bcc for systems with low SFE ( $< 20$  mJm $^{-2}$ )[14,50,53] whereas  $\gamma$ -fcc  $\rightarrow$   $\alpha'$ -bcc was observed with systems with high SFE ( $> 20$  mJm $^{-2}$ )[14,49,50]. Recently, Polatidis et al.[48,54,55] studied the effect of uniaxial and biaxial loading on martensitic transformation in low SFE austenitic stainless steel (ASS). The martensitic sequence was  $\gamma$ -fcc  $(111) \rightarrow \varepsilon$ -hcp  $(10\bar{1}1) \rightarrow \alpha'$ -bcc  $(110)$ , where  $\varepsilon$ -hcp was a precursor for the nucleation of  $\alpha'$ -bcc.

These studies motivated us to initiate the understanding of hcp to bcc transformation due to deformation and ways to promote such hcp intersections that result in the nucleation of the bcc phase for the present case. Sample C is selected for this study after deformation where the total strain attained before fracture was 15%. An area in the sample is selected to cover grains with different V content, as shown in Figure 8. It was assured that the regions/grains selected did undergo deformation, as the objective was to explore strain-induced nucleation of  $\alpha$ -bcc. It was confirmed by the presence of multiple slips in all the images, the indication of high deformation experienced by that particular grain.

Figure 8 (a) shows an EDS map of the region selected showing varying V content with an average of 2.54 at.%. The regions for microscopy were selected based on the local composition of the grains carried out by EDS spot analysis. Figure 8 (b), an SEM-BSE image, shows regions selected for EDS spot analysis based on the information established through Figures 3 to 6, for the phases with different contrast. Figure 8 (c) is the magnified view of the area bounded by dashed lines in Figure 8 (b), for better visibility of the EDS spots and phases. As can be noted, spot 1 is very near to the V rich region and spot 3 is in the matrix with grey contrast, whereas spots from 4-8 are from regions with a matrix with brighter contrast and with fine grains. Spots 11-16, marked with small squares, are regions that were selected for further microscopy to study the transformation via EBSD, to identify the orientation of the grain and phases present. Figure 8 (d) is the EDS composition map for V from Figure 8 (a<sub>1</sub>) with the exact area marked for further EBSD. Figure 8 (f) gives the quantification of the spot analysis from Figures 8 (b) and (e) while comparing it with the base alloy Cu-HEA.

Figure 9 is for regions 13-16 with medium V content in the range of 0.76-1.03 at.% (Figure 8 (f)). Figure 9 (a) is the SEM-BSE image to specify the regions in solid enclosures for analysis. Figure

9 (b) is the region with V around 0.8 at.%. The sequence followed for cataloging each region was, 1) inverse pole figure (IPF) map, 2) phase map where the green color is for  $\gamma$ -fcc, red is for  $\varepsilon$ -hcp and yellow is for  $\alpha$ -bcc, 3)  $\alpha$ -bcc phase map, and 4) image quality (IQ) map. IPF map (Figure 9 (b<sub>1</sub>)) shows the  $\gamma$ -fcc grains 1 and 2 at or near {111} orientation showing the presence of  $\alpha$ -bcc nucleation as seen from  $\alpha$ -bcc phase map (Figure 9 (b<sub>3</sub>)) inside the  $\varepsilon$ -hcp laths with near {10 $\bar{1}$ 1} orientation (Figures 9 (b<sub>1</sub>) and (b<sub>2</sub>)). A similar observation of  $\alpha$ -bcc being inside the  $\varepsilon$ -hcp phase was reported by Polatidis et al.[48]. The IQ image (Figure 9 (b<sub>4</sub>)) shows the {111} slip traces of  $\gamma$ -fcc in dashed lines. The yellow traces correspond to positive nucleation of  $\alpha$ -bcc whereas blue traces show no evidence of  $\alpha$ -bcc. Figure 9 (c) is for a region with V around 0.78 at.% with observations similar to Figure 9 (b). An additional interesting observation was the nucleation of  $\varepsilon$ -hcp with basal orientation {0001} from the intersecting  $\varepsilon$ -hcp planes with pyramidal {10 $\bar{1}$ 1} orientation in parent  $\gamma$ -fcc {111} orientation. These observations are seen in grains 2 and 4 (Figure 9 (c<sub>1</sub>)) where the basal oriented  $\varepsilon$ -hcp is encircled with a dashed yellow circle and the {111}. As seen from Figure 9 (c<sub>4</sub>), the IQ map, not all {111} traces leads to  $\alpha$ -bcc nucleation. The ones with yellow traces show the evidence of  $\alpha$ -bcc nucleation. The reason could be the orientation of the parent  $\gamma$ -fcc grain and the  $\frac{1}{6}\langle\bar{1}2\bar{1}\rangle$  partials with respect to the tensile axis. The orientation with respect to the tensile axis will determine the Schmid factor of the leading and the trailing partials and thus the separation between the partials[15,23,48,56], determining the nucleation of  $\varepsilon$ -hcp and thus  $\alpha$ -bcc. The mechanism from fcc to hcp has been widely discussed[15] and from hcp to bcc is explained by Bogers and Burgers[49] and is not repeated in this paper. The observations from each grain for a particular region are listed in the figure itself. Figure 9 (d) is for region enclosed in yellow in Figure 9 (a) with an average V content of 0.76 at.%. This image reiterates that high strain

levels evidenced by multiple slip with deep slip lines are required to nucleate  $\alpha$ -bcc inside  $\varepsilon$ -hcp.

Figure 9 (e) captures a coarse  $\{111\}$  oriented  $\gamma$ -fcc grain where basal oriented  $\varepsilon$ -hcp was observed at the intersection node of  $\varepsilon$ -hcp of pyramidal planes, as seen in the magnified image in Figure 9 (e<sub>5</sub>). The average V content of the region was around 1.03 at.% with the activation of multiple slip. The grains 2 and 4, with off  $\{111\}$  orientation as seen from Figure 9 (e<sub>1</sub>) do not lead to  $\alpha$ -bcc nucleation. For the grain 3, the orientation of  $\gamma$ -fcc is near to  $\{112\}$  leading to  $\alpha$ -bcc nucleation on near  $\{2\bar{1}\bar{1}1\}$  pyramidal twin plane of  $\varepsilon$ -hcp. Figure 9 summarizes a) the average V composition of around 0.7-1 at.% with parent  $\gamma$ -fcc orientation at or near  $\{111\}$  leading to nucleation of  $\alpha$ -bcc inside  $\varepsilon$ -hcp orientated for the pyramidal slip, and (b) the  $\varepsilon$ -hcp with basal orientation is nucleated at the intersection node of  $\varepsilon$ -hcp with pyramidal orientation.

Similar analysis as Figure 9 (with medium V content) was carried out for regions with higher V content and low V, as seen in Figure 10. Figure 10 (a) is the SEM-BSE image with red, orange, and pink enclosures with higher V content used for analysis. Figure 10 (b) is for the region in the range of 1.5-9 at.%. As marked in Figure 10 (b<sub>3</sub>), the region with V content > 9 at.% is seen to give a fine-grained  $\varepsilon$ -hcp (Figures 10 (b<sub>2</sub>) and (b<sub>4</sub>)). Near to the  $\varepsilon$ -hcp band (Figures 10 (b<sub>1</sub>) and (b<sub>4</sub>)), there are grains with not so deep slip lines suggesting the maximum share of the load during straining taken by  $\varepsilon$ -hcp instead of the  $\gamma$ -fcc phase. The region has a coarse  $\gamma$ -fcc grains with near  $\{111\}$  slip and with V content around 1.6 at.%, no evidence of  $\alpha$ -bcc, as seen from Figure 10 (b<sub>3</sub>). The argument is that 1.6 at.% of V too could promote the nucleation of  $\alpha$ -bcc, but due to the maximum load shared by the  $\varepsilon$ -hcp phase, these grain did not undergo deformation to strain levels required for the nucleation of  $\alpha$ -bcc. The region with V content great than 2.3 at.% as shown in Figure 10 (b<sub>3</sub>) shows fine  $\gamma$ -fcc grains with no trace of  $\alpha$ -bcc except the grain boundaries which

could be the mis-indexed points. Figure 10 (c) is for a region with finer  $\gamma$ -fcc grains, the recrystallized strain-free strains, due to the FSP. The V content of this region is in the range of 2.5-3.5 at.%. Due to the recrystallized grains, the nucleation of  $\alpha$ -bcc did not take place. Again Figure 10 (d) is for varying V content, in the range of 0.8-8.2 at.%. In the region with 2.5-3.5 at.% V, the grains with multiple slips did not show any evidence of  $\alpha$ -bcc nucleation and the one with around 8.2 at.% V lead to  $\varepsilon$ -hcp phase as seen from Figures 10 (d<sub>2</sub>)-(d<sub>4</sub>). The region with 0.8-0.98 at.% showed traces of  $\alpha$ -bcc with  $\gamma$ -fcc grains orientated to near {111} slip. Figure 10 (e) is the region with low V content around 0.04 at.%. Although there are multiple slips observed as seen from Figure 10 (e) and the IQ map in Figure 10 (e<sub>4</sub>), there is no evidence of  $\alpha$ -bcc nucleation (Figure 10 (e<sub>3</sub>)) even for the preferentially orientated grain for {111} slip (Figure 10 (e<sub>1</sub>)). From Figure 9 or 10, there was no evidence of  $\alpha$ -bcc nucleating directly from  $\gamma$ -fcc, suggesting the martensitic sequence to be  $\gamma$ -fcc  $\rightarrow$   $\varepsilon$ -hcp  $\rightarrow$   $\alpha$ -bcc, reported for parent  $\gamma$ -fcc systems with low SFE.

The XRD results from Figure 2 (b) provide evidence for the presence of  $\alpha$ -bcc (110) and (211) peaks. An increase in peak intensity of (110)  $\alpha$ -bcc along with (10 $\bar{1}$ 1)  $\varepsilon$ -hcp peaks was reported by Polatidis et. al[55] for uniaxial deformation of ASS via neutron diffraction. To confirm the presence of  $\alpha$ -bcc, further TEM was done on specific samples, as shown in Figure 11. Figure 11a is for the sample milled from the high V region (sample C, Figure 5 (c)) for the chemistry effect. Figure 11 (a<sub>1</sub>) shows the phase map where yellow grains correspond to the  $\alpha$ -bcc phase whereas Figure 11 (a<sub>2</sub>) is the corresponding virtual bright field image. To verify the strain-induced nucleation of  $\alpha$ -bcc, the TEM sample was milled from the region marked as grain 2 in Figure 9 (b<sub>1</sub>). Figure 11 (b<sub>1</sub>) is the virtual-dark field image where PED was carried out in the region enclosed by a white rectangle. Comparing Figures 11 (b<sub>2</sub>) and (b<sub>3</sub>), corresponding to orientation and phase

maps, the  $\gamma$ -fcc (green) phase has  $\{111\}$  orientation with  $\varepsilon$ -hcp (red) with  $\{10\bar{1}1\}$  and  $\alpha$ -bcc with  $\{101\}$  orientation. Figures 11 (b<sub>4</sub>), (b<sub>5</sub>) and (b<sub>6</sub>) are diffraction patterns confirming the orientation relationship of  $\{111\}_\gamma \parallel \{10\bar{1}1\}_\varepsilon \parallel \{101\}_\alpha$  and  $\langle 10\bar{1} \rangle_\gamma \parallel \langle 0\bar{1}11 \rangle_\varepsilon \parallel \langle 1\bar{1}1 \rangle_\alpha$ . This shows that the nucleation of (110)  $\alpha$ -bcc is from nucleation of (10 $\bar{1}$ 1)  $\varepsilon$ -hcp with (111)  $\gamma$ -fcc as the parent phase with deformation, as reported in the literature[14,48,54,55].

Figure 12 gives the key points from the present work where FSGA, a HT technique leads to the generation of a library of composition and microstructure, providing guidance for selection of suitable levels of V concentration, ~1 at.%, to enable the nucleation of  $\alpha$ -bcc. The martensitic sequence was established for this low SFE  $\gamma$ -fcc dominated HEA, with the details of the dual effect of chemistry and strain along with the preferred orientation of nucleation of the daughter phase from the parent phase ( $\varepsilon$ -hcp from  $\gamma$ -fcc and  $\alpha$ -bcc from  $\varepsilon$ -hcp).

#### 4. Summary

Friction stir gradient alloying, a high-throughput technique was used to create a library of composition and microstructure to explore the evolution of the  $\alpha$ -bcc phase with V addition, in a transforming high entropy alloy with dominant  $\gamma$ -fcc phase.

- The study established around 1 at.% V needed with  $\{111\}$   $\gamma$ -fcc orientated parent phase for the evolution of  $\alpha$ -bcc.
- The present work is the first to study the dual effect of chemistry and strain resulting in the co-existence of all three phases (fcc, hcp and bcc).

- During deformation,  $\gamma$ -fcc to  $\varepsilon$ -hcp transformation in HEAs is well-documented and attributed to the TRIP effect. The current study is the first in HEAs to explore the nucleation of the  $\alpha$ -bcc phase in the vicinity of  $\varepsilon$ -hcp orientated for the pyramidal slip.
- Additional evidence of nucleation of  $\varepsilon$ -hcp with basal orientation were reported at the nodes of intersecting  $\{10\bar{1}1\}$   $\varepsilon$ -hcp planes due to strain.
- The sequence to the formation of martensite was established to  $\gamma$ -fcc (111)  $\rightarrow$   $\varepsilon$ -hcp (10 $\bar{1}$ 1)  $\rightarrow$   $\alpha$ -bcc, where  $\varepsilon$ -hcp is the predecessor for the formation of  $\alpha$ -bcc.

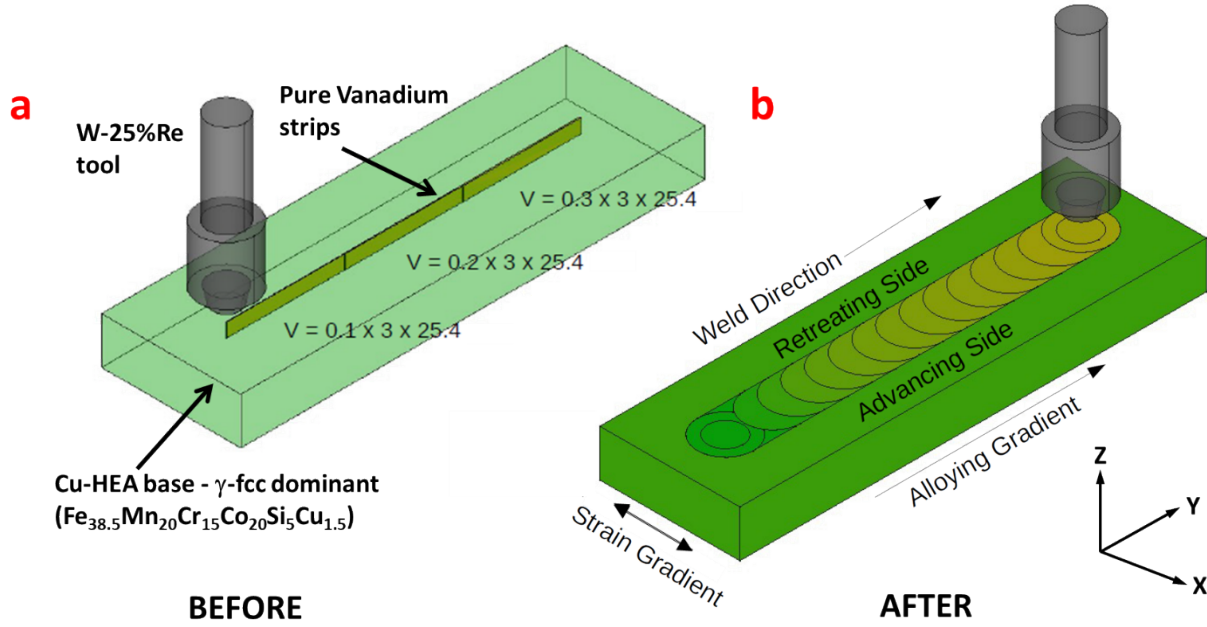


Figure 1. Schematic of friction stir gradient alloying (FSGA) assembly with Cu-HEA as the base material and pure V strips with different thickness (dimensions in mm) used for alloying (a) before FSGA, and (b) after FSGA with alloy gradient parallel to the weld direction.

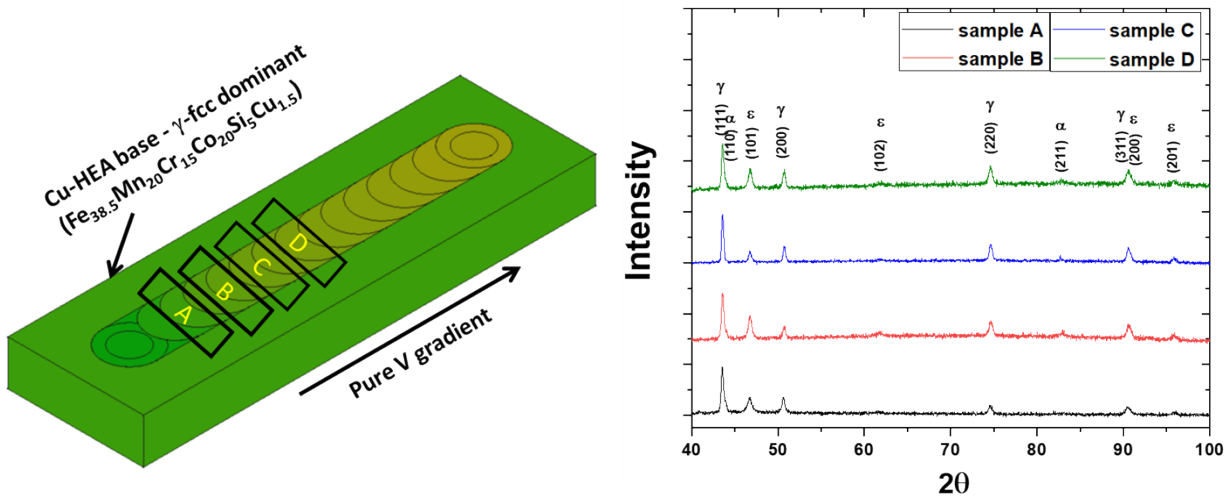


Figure 2. (a) Schematic of the location where the samples were milled out for testing and microscopy, and (b) X-ray diffraction plots of intensity vs.  $2\theta$  (Bragg's angle) for all the as-FSGA samples. Diffraction peaks are indexed along with the corresponding phase:  $\gamma$ -fcc,  $\epsilon$ -hcp and  $\alpha$ -bcc.

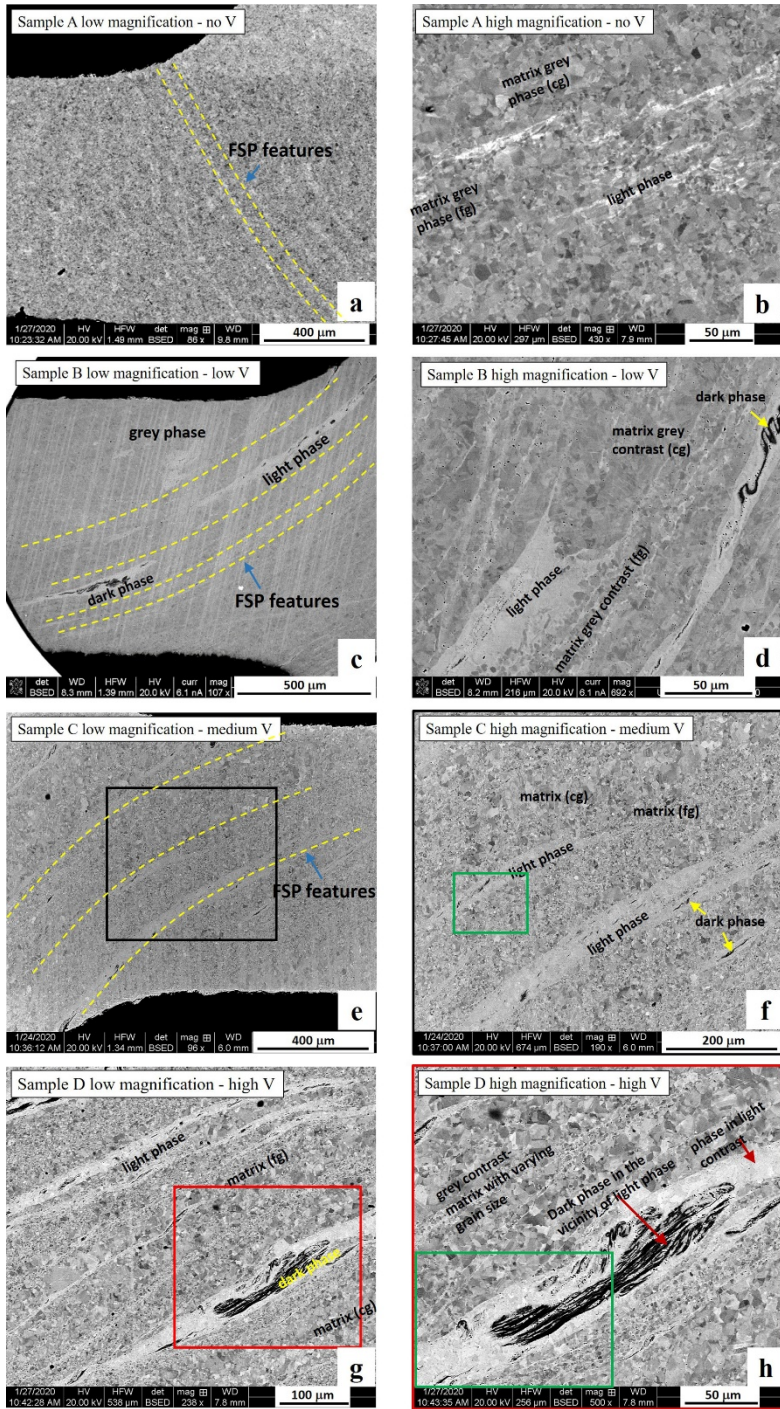


Figure 3. SEM-BSE images for as-FSGA processed samples with different V content (a) low magnification image from sample A, (b) high magnification image from sample A with no dark phase, (c) low magnification image from sample B with phases in different contrast labeled along with the FSP features, (d) high magnification image from sample B, (e) low magnification image for sample C, (f) high magnification image for sample C, (g) low magnification image for sample D with a high fraction of phase in dark contrast, and (h) high magnification image for sample D. Note: cg is for coarse grain and fg is for fine grain.

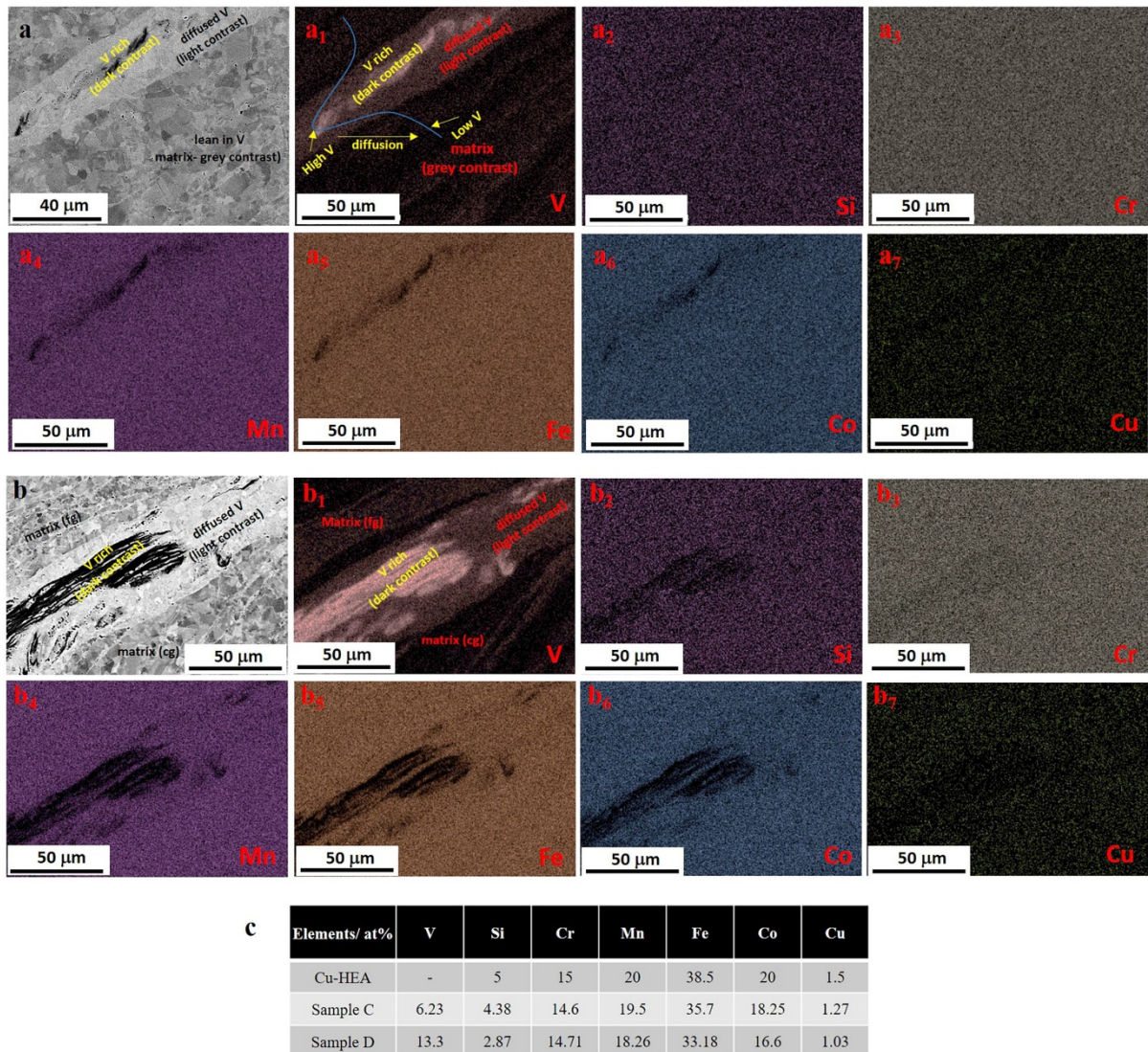


Figure 4. SEM-EDS for high V content samples. Sample C: (a) SEM-BSE image, (a<sub>1</sub>) V map, (a<sub>2</sub>) Si map, (a<sub>3</sub>) Cr map, (a<sub>4</sub>) Mn map, (a<sub>5</sub>) Fe map, (a<sub>6</sub>) Co map, and (a<sub>7</sub>) Cu map. Sample D: (b) SEM-BSE image, (b<sub>1</sub>) V map, (b<sub>2</sub>) Si map, (b<sub>3</sub>) Cr map, (b<sub>4</sub>) Mn map, (b<sub>5</sub>) Fe map, (b<sub>6</sub>) Co map, (b<sub>7</sub>) Cu map, and (c) summary of the at.% fraction of the elements present in both C and D samples and comparison with the nominal composition of the base Cu-HEA.

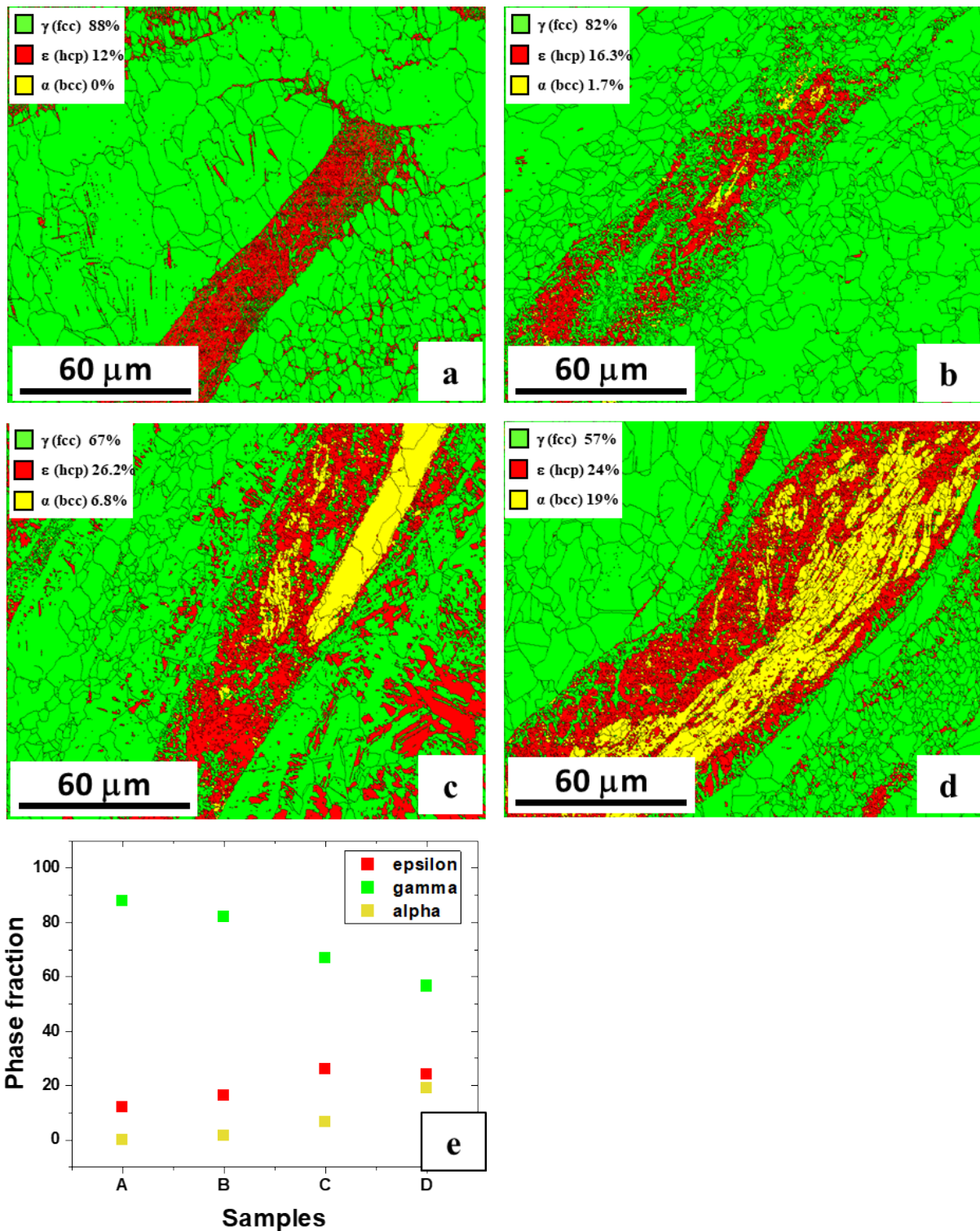


Figure 5. EBSD phase maps for (a) sample A, (b) sample B, (c) sample C, and (d) sample D, and (e) phase fraction for different samples.

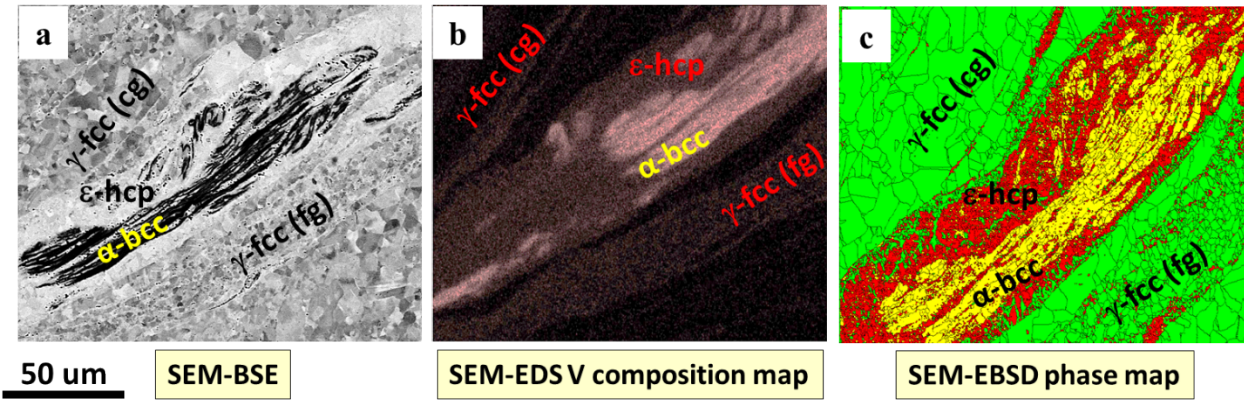


Figure 6. SEM comparison study (a) BSE image, (b) EDS composition map for V, and (c) EBSD phase map. Note: the micron bar is the same for all the three images.

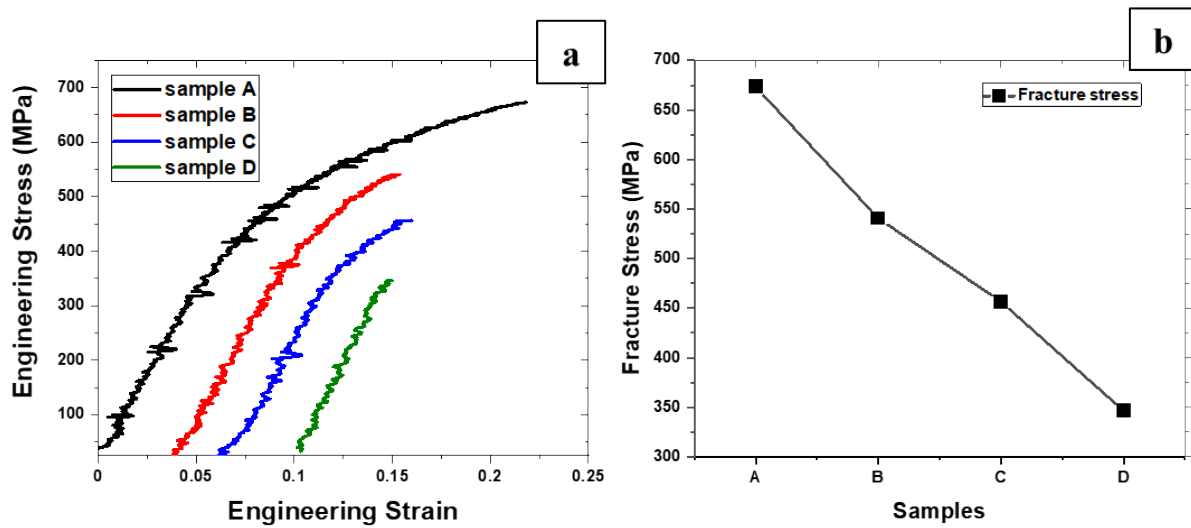


Figure 7. (a) Tensile engineering stress-strain curves comparing friction stir processed samples with the control sample A (the curves have been shifted horizontally for clarity), and (b) trend of fractures with an increase in V content.

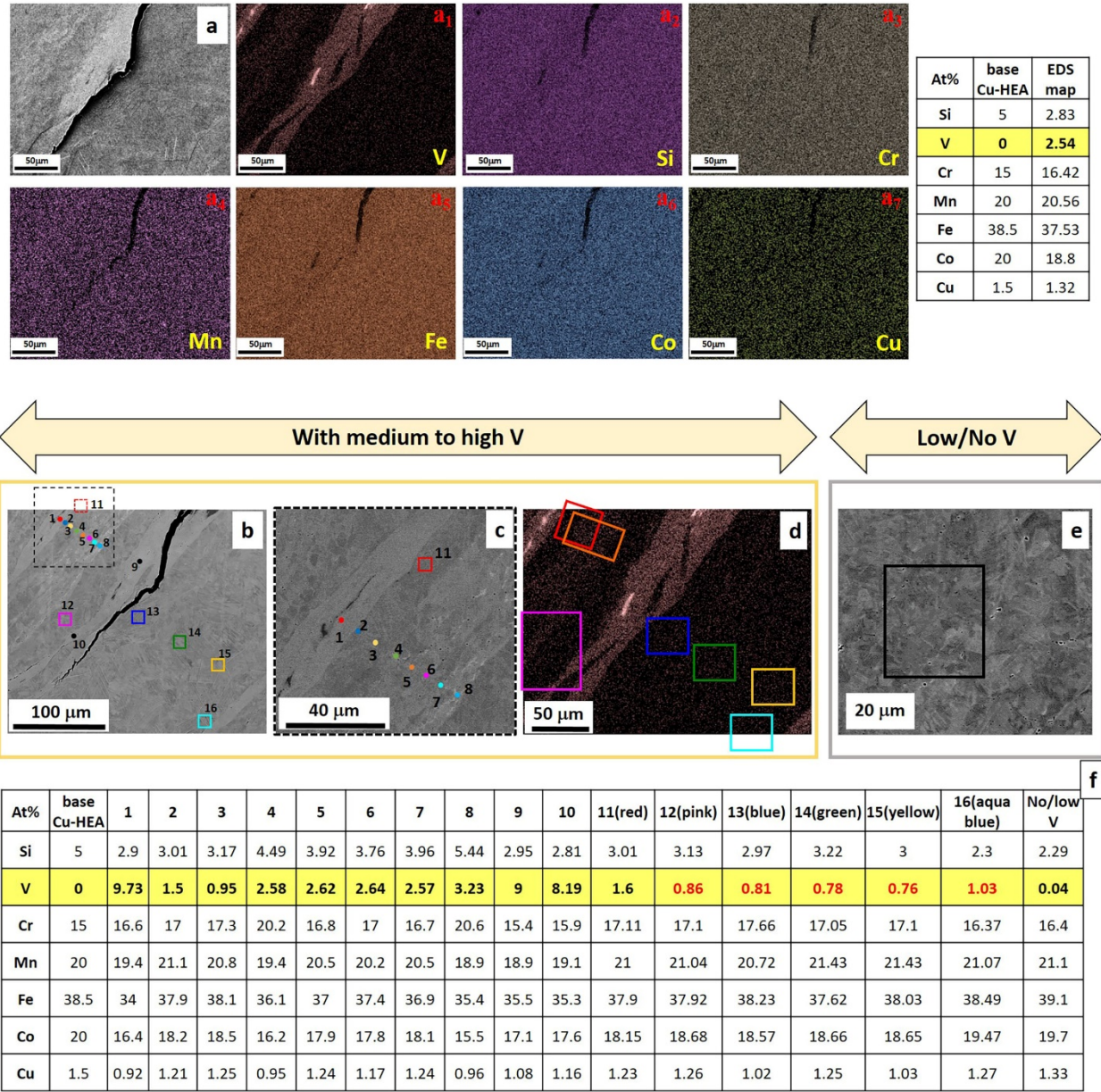


Figure 8. EDS analysis of the region selected for further detailed microscopy with varying V content, (a) composition map, (b) spot analysis, (c) magnified view of an area in (b), (d) superimposition of V composition map with areas narrowed down for EBSD analysis, (e) region with very low V content, and (f) quantification of the spot EDS composition analysis in at.%

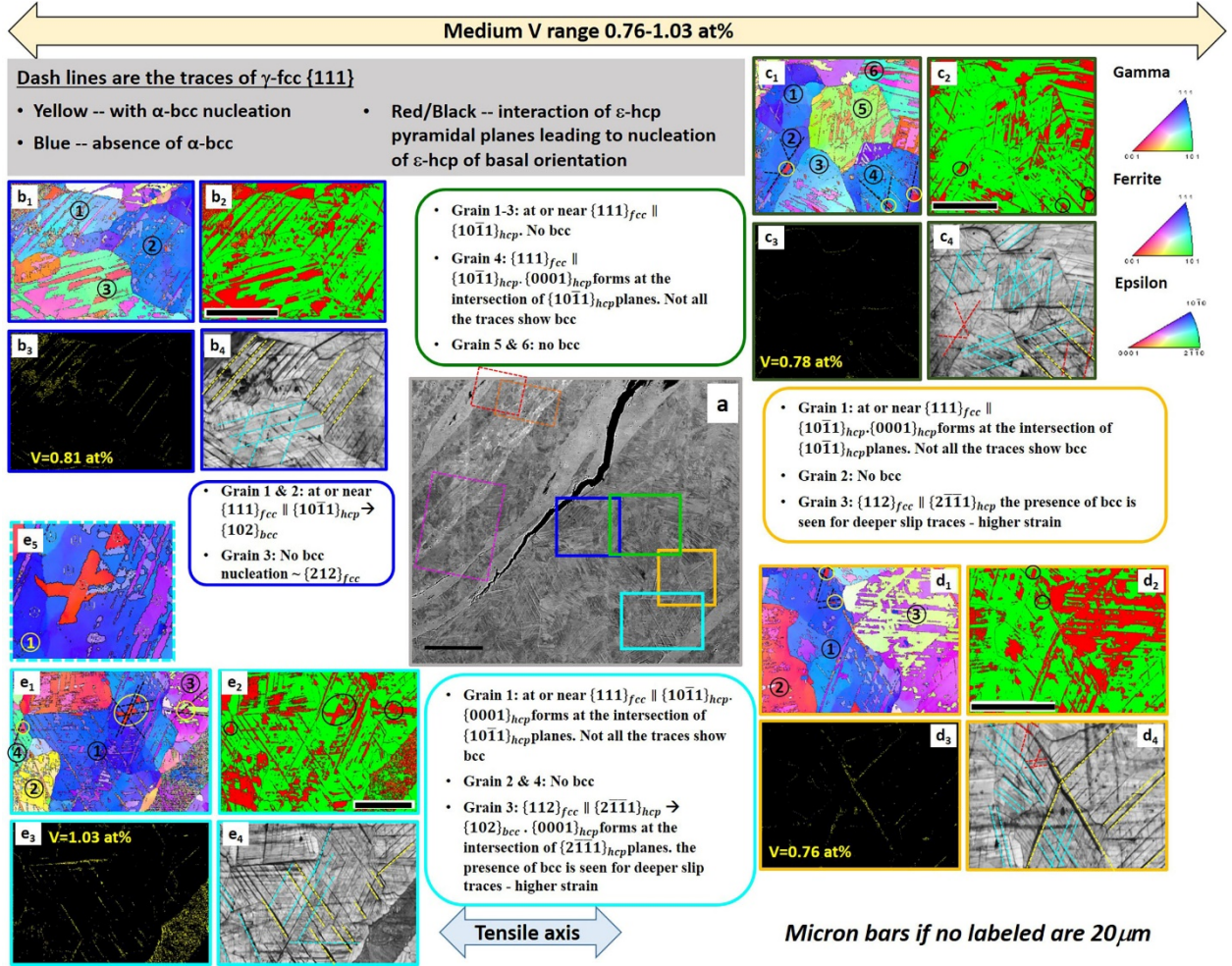


Figure 9. EBSD analysis for medium V content 0.76-1.03 at%. (a) SEM-BSE image marking the region for analysis in solid enclosure; (b) V ~0.81at.%, (b<sub>1</sub>) IPF map, (b<sub>2</sub>) phase map, (b<sub>3</sub>)  $\alpha$ -bcc phase map, (b<sub>4</sub>) IQ map; (c) V ~0.78 at.%, (c<sub>1</sub>) IPF map, (c<sub>2</sub>) phase map, (c<sub>3</sub>)  $\alpha$ -bcc phase map, (c<sub>4</sub>) IQ map; (d) V ~0.76 at.%, (d<sub>1</sub>) IPF map, (d<sub>2</sub>) phase map, (d<sub>3</sub>)  $\alpha$ -bcc phase map, and (d<sub>4</sub>) IQ map, (e) V ~1.03 at.%, (e<sub>1</sub>) IPF map, (e<sub>2</sub>) phase map, (e<sub>3</sub>)  $\alpha$ -bcc phase map, and (e<sub>4</sub>) IQ map, and (e<sub>5</sub>) magnified view of region enclosed with dashed square in (e<sub>1</sub>) to show nucleation of basal oriented  $\varepsilon$ -hcp from  $\varepsilon$ -hcp oriented for pyramidal slip.

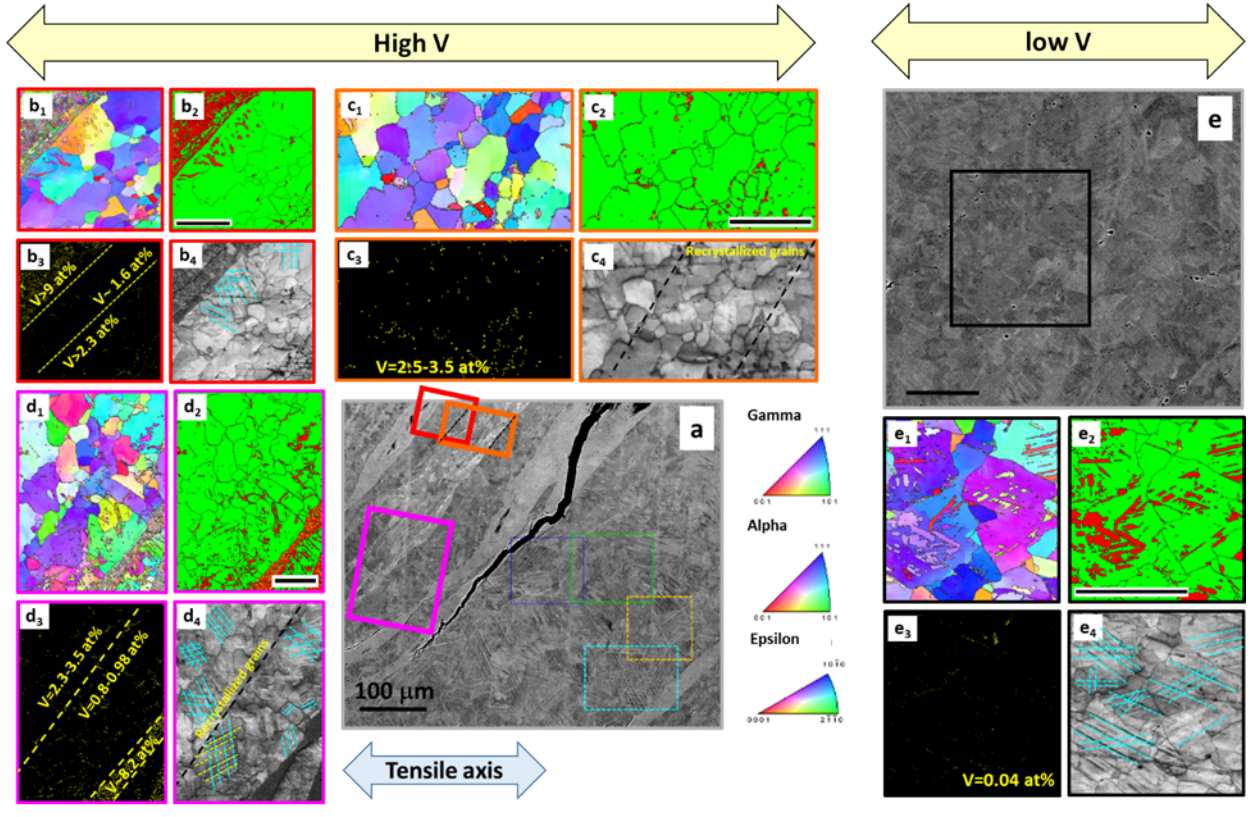


Figure 10. EBSD analysis for higher and lower V content. **High V:** (a) SEM-BSE image marking the region for analysis in solid enclosure; (b) V range from 1.6 to <9 at.%, (b<sub>1</sub>) IPF map, (b<sub>2</sub>) phase map, (b<sub>3</sub>)  $\alpha$ -bcc phase map, (b<sub>4</sub>) IQ map; (c) V range from 2.5-3.5 at.%, (c<sub>1</sub>) IPF map, (c<sub>2</sub>) phase map, (c<sub>3</sub>)  $\alpha$ -bcc phase map, (c<sub>4</sub>) IQ map; (d) V range from 0.8-8.2 at.%, (d<sub>1</sub>) IPF map, (d<sub>2</sub>) phase map, (d<sub>3</sub>)  $\alpha$ -bcc phase map, and (d<sub>4</sub>) IQ map. **Low V:** (e) SEM-BSE image for region with low V, (e<sub>1</sub>) IPF map from the region enclosed in black rectangle in (e), (e<sub>2</sub>) phase map, (e<sub>3</sub>)  $\alpha$ -bcc phase map, and (e<sub>4</sub>) IQ map.

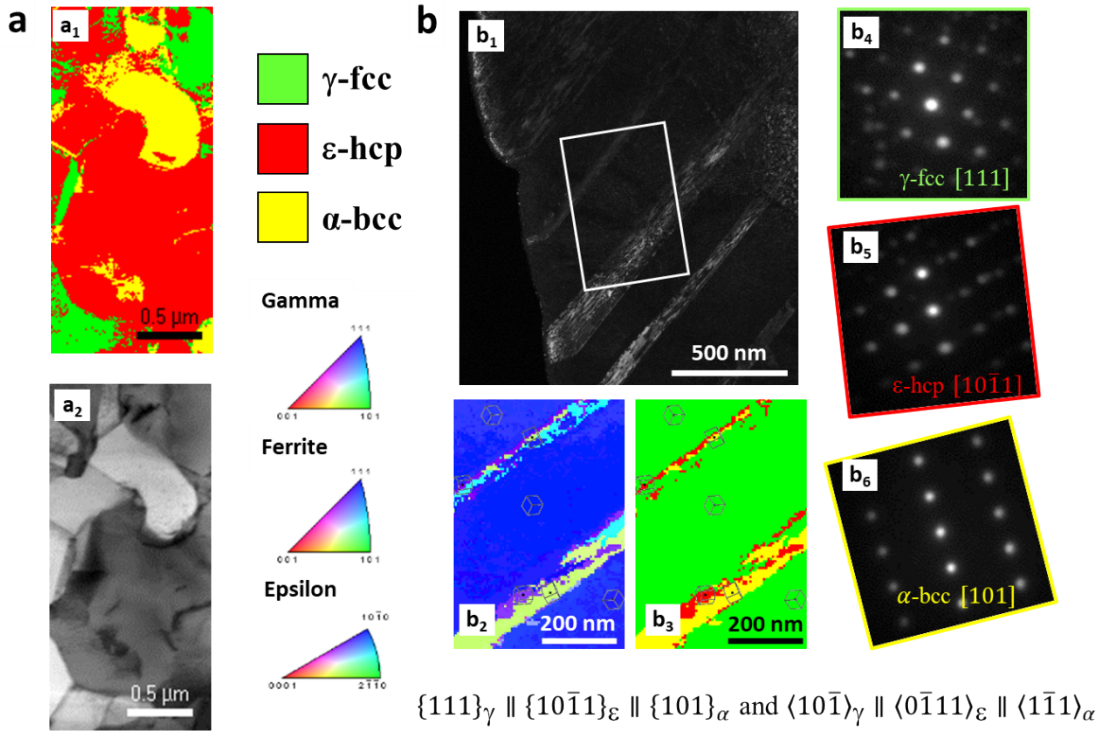


Figure 11: TEM analysis to confirm the presence of  $\alpha$ -bcc (a) chemistry effect: (a<sub>1</sub>) phase map, (a<sub>2</sub>) virtual bright-field image, (b) strain effect (sample milled from grain 2 of Figure 9 (b<sub>1</sub>): (b<sub>1</sub>) virtual dark field image (OIM), (b<sub>2</sub>) orientation image map (OIM), (b<sub>3</sub>) phase map, (b<sub>4</sub>) [111] zone axis of  $\gamma$ -fcc, (b<sub>5</sub>) [10 $\bar{1}$ 1] zone axis of  $\varepsilon$ -hcp, and (b<sub>6</sub>) [101] zone axis of  $\alpha$ -bcc

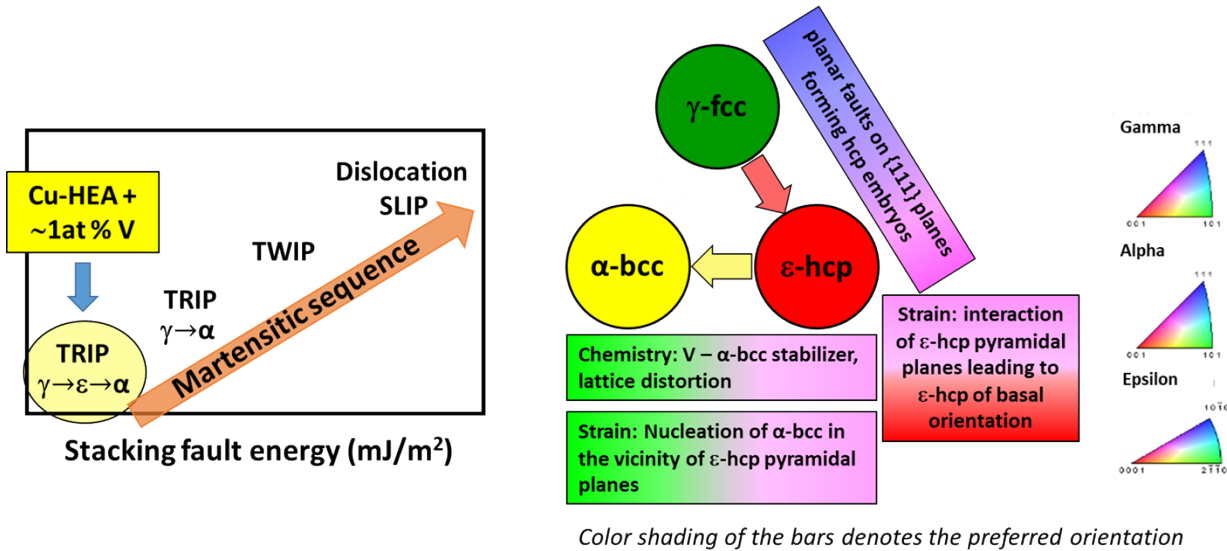


Figure 12. Key results from the current work. Around 1 at.% V is needed in Cu-HEA to result in the nucleation of  $\alpha$ -bcc with  $\varepsilon$ -hcp as the precursor, with the martensitic sequence of  $\gamma$ -fcc (111)  $\rightarrow$   $\varepsilon$ -hcp (10 $\bar{1}$ 1)  $\rightarrow$   $\alpha'$ -bcc (110) for this low SFE HEA.

## References

- [1] B. Cantor, I.T.H. Chang, P. Knight, A.J.B. Vincent, Microstructural development in equiatomic multicomponent alloys, *Mater. Sci. Eng. A.* 375–377 (2004) 213–218. <https://doi.org/10.1016/j.msea.2003.10.257>.
- [2] J.-W. Yeh, S.-K. Chen, S.-J. Lin, J.-Y. Gan, T.-S. Chin, T.-T. Shun, C.-H. Tsau, S.-Y. Chang, Nanostructured High-Entropy Alloys with Multiple Principal Elements: Novel Alloy Design Concepts and Outcomes, *Adv. Eng. Mater.* 6 (2004) 299–303. <https://doi.org/10.1002/adem.200300567>.
- [3] S. Ranganathan, Alloyed pleasures: Multimetallic cocktails, *Curr. Sci.* 85 (2003) 1404–1406.
- [4] D.B. Miracle, O.N. Senkov, A critical review of high entropy alloys and related concepts, *Acta Mater.* 122 (2017) 448–511. <https://doi.org/10.1016/j.actamat.2016.08.081>.
- [5] B.S. Murty, High-Entropy Alloys, n.d.
- [6] E.P. George, D. Raabe, R.O. Ritchie, High-entropy alloys, *Nat. Rev. Mater.* 4 (2019) 515–534. <https://doi.org/10.1038/s41578-019-0121-4>.
- [7] S. Shukla, T. Wang, S. Cotton, R.S. Mishra, Hierarchical microstructure for improved fatigue properties in a eutectic high entropy alloy, *Scr. Mater.* 156 (2018) 105–109. <https://doi.org/10.1016/j.scriptamat.2018.07.022>.
- [8] S. Shukla, D. Choudhuri, T. Wang, K. Liu, R. Wheeler, S. Williams, B. Gwalani, R.S. Mishra, Hierarchical features infused heterogeneous grain structure for extraordinary strength-ductility synergy, (2018). <https://doi.org/10.1080/21663831.2018.1538023>.
- [9] Y. Deng, C.C. Tasan, K.G. Pradeep, H. Springer, A. Kostka, D. Raabe, Design of a twinning-induced plasticity high entropy alloy, *Acta Mater.* 94 (2015) 124–133. <https://doi.org/10.1016/j.actamat.2015.04.014>.
- [10] S. Shukla, R.S. Mishra, Excellent high cyclic fatigue properties of a novel ultrafine-grained medium entropy alloy, *Mater. Sci. Eng. A.* 779 (2020) 139122. <https://doi.org/10.1016/j.msea.2020.139122>.
- [11] Y. Lu, X. Gao, L. Jiang, Z. Chen, T. Wang, J. Jie, H. Kang, Y. Zhang, S. Guo, H. Ruan, Y. Zhao, Z. Cao, T. Li, Directly cast bulk eutectic and near-eutectic high entropy alloys with balanced strength and ductility in a wide temperature range, *Acta Mater.* 124 (2017) 143–150. <https://doi.org/10.1016/j.actamat.2016.11.016>.
- [12] Y. Lu, Y. Dong, S. Guo, L. Jiang, H. Kang, T. Wang, B. Wen, Z. Wang, J. Jie, Z. Cao, H. Ruan, T. Li, A promising new class of high-temperature alloys: Eutectic high-entropy alloys, *Sci. Rep.* 4 (2014) 1–5. <https://doi.org/10.1038/srep06200>.
- [13] Z. Li, D. Raabe, Strong and Ductile Non-equiatomic High-Entropy Alloys: Design, Processing, Microstructure, and Mechanical Properties, *JOM.* 69 (2017) 2099–2106. <https://doi.org/10.1007/s11837-017-2540-2>.
- [14] G.B. Olson, M. Cohen, A mechanism for the strain-induced nucleation of martensitic transformations, *J. Less-Common Met.* 28 (1972) 107–118. [https://doi.org/10.1016/0022-5088\(72\)90173-7](https://doi.org/10.1016/0022-5088(72)90173-7).

- [15] G.B. Olson, M. Cohen, A general mechanism of martensitic nucleation: Part I. General Concepts and the FCC-HCP Transformation, *Metall. Trans. A.* 7 (1976) 1915–1923. <https://doi.org/10.1007/BF02654989>.
- [16] G.B. Olson, M. Cohen, A general mechanism of martensitic nucleation: Part II. FCC→BCC and other martensitic transformations, *Metall. Trans. A.* 7 (1976) 1905–1914. <https://doi.org/10.1007/BF02654988>.
- [17] B. Yin, F. Maresca, W.A. Curtin, Vanadium is an optimal element for strengthening in both fcc and bcc high-entropy alloys, *Acta Mater.* (2020). <https://doi.org/10.1016/j.actamat.2020.01.062>.
- [18] S.S. Nene, K. Liu, M. Frank, R.S. Mishra, R.E. Brennan, K.C. Cho, Z. Li, D. Raabe, Enhanced strength and ductility in a friction stir processing engineered dual phase high entropy alloy, *Sci. Rep.* 7 (2017) 1–7. <https://doi.org/10.1038/s41598-017-16509-9>.
- [19] S.S. Nene, M. Frank, K. Liu, R.S. Mishra, B.A. McWilliams, K.C. Cho, Extremely high strength and work hardening ability in a metastable high entropy alloy, *Sci. Rep.* 8 (2018). <https://doi.org/10.1038/s41598-018-28383-0>.
- [20] S.S. Nene, M. Frank, K. Liu, S. Sinha, R.S. Mishra, B. McWilliams, K.C. Cho, Reversed strength-ductility relationship in microstructurally flexible high entropy alloy, *Scr. Mater.* 154 (2018) 163–167. <https://doi.org/10.1016/j.scriptamat.2018.05.043>.
- [21] S.S. Nene, S. Sinha, M. Frank, K. Liu, R.S. Mishra, B.A. McWilliams, K.C. Cho, Unexpected strength-ductility response in an annealed, metastable, high-entropy alloy, *Appl. Mater. Today.* 13 (2018) 198–206. <https://doi.org/10.1016/j.apmt.2018.09.002>.
- [22] M. Frank, Y. Chen, S.S. Nene, S. Sinha, K. Liu, K. An, R.S. Mishra, Investigating the deformation mechanisms of a highly metastable high entropy alloy using in-situ neutron diffraction, *Mater. Today Commun.* (2020). <https://doi.org/10.1016/j.mtcomm.2019.100858>.
- [23] S. Sinha, S.S. Nene, M. Frank, K. Liu, P. Agrawal, R.S. Mishra, On the evolving nature of c/a ratio in a hexagonal close-packed epsilon martensite phase in transformative high entropy alloys, *Sci. Rep.* 9 (2019). <https://doi.org/10.1038/s41598-019-49904-5>.
- [24] Sanya Gupta, S.S. Nene, P. Agrawal, R.S. Mishra, Enhanced joint efficiency and strength metastable high entropy alloy using friction stir welding, (n.d.).
- [25] S.S. Nene, M. Frank, P. Agrawal, S. Sinha, K. Liu, S. Shukla, R.S. Mishra, B.A. McWilliams, K.C. Cho, Microstructurally flexible high entropy alloys: Linkages between alloy design and deformation behavior, *Mater. Des.* 194 (2020) 108968. <https://doi.org/10.1016/j.matdes.2020.108968>.
- [26] S. Shukla, T. Wang, M. Frank, P. Agrawal, S. Sinha, R.A. Mirshams, R.S. Mishra, Friction stir gradient alloying: A novel solid-state high throughput screening technique for high entropy alloys, *Mater. Today Commun.* 23 (2020) 100869. <https://doi.org/10.1016/j.mtcomm.2019.100869>.
- [27] R.S. Mishra, Z.Y. Ma, Friction stir welding and processing, *Mater. Sci. Eng. R Reports.* 50 (2005) 1–78. <https://doi.org/10.1016/j.mser.2005.07.001>.
- [28] T.H. Fang, W.L. Li, N.R. Tao, K. Lu, Revealing extraordinary intrinsic tensile plasticity in

- gradient nano-grained copper, *Science* (80- ). 331 (2011) 1587–1590. <https://doi.org/10.1126/science.1200177>.
- [29] K. Lu, Making strong nanomaterials ductile with gradients, *Science* (80- ). 345 (2014) 1455–1456. <https://doi.org/10.1126/science.1255940>.
- [30] J. Fan, L. Zhu, J. Lu, T. Fu, A. Chen, Theory of designing the gradient microstructured metals for overcoming strength-ductility trade-off, *Scr. Mater.* 184 (2020) 41–45. <https://doi.org/10.1016/j.scriptamat.2020.03.045>.
- [31] L. Zhai, Y. Lu, X. Zhao, L. Wang, X. Lu, High-throughput screening of laser additive manufactured metallic glass via ultrasonic wave, *Sci. Rep.* 9 (2019) 1–6. <https://doi.org/10.1038/s41598-019-54293-w>.
- [32] S. Guerin, B.E. Hayden, Physical vapor deposition method for the high-throughput synthesis of solid-state material libraries, *J. Comb. Chem.* 8 (2006) 66–73. <https://doi.org/10.1021/cc050117p>.
- [33] S.S. Nene, M. Frank, P. Agrawal, S. Sinha, K. Liu, S. Shukla, R.S. Mishra, B. McWilliams, K. Cho, Microstructurally Flexible High Entropy Alloys: Linkages Between Alloy Design and Deformation Behavior, *Acta Mater.* (n.d.).
- [34] S.S. Nene, M. Frank, K. Liu, S. Sinha, R.S. Mishra, B.A. McWilliams, K.C. Cho, Corrosion-resistant high entropy alloy with high strength and ductility, *Scr. Mater.* 166 (2019) 168–172. <https://doi.org/10.1016/j.scriptamat.2019.03.028>.
- [35] K. Liu, S.S. Nene, M. Frank, S. Sinha, R.S. Mishra, Extremely high fatigue resistance in an ultrafine grained high entropy alloy, *Appl. Mater. Today.* 15 (2019) 525–530. <https://doi.org/10.1016/j.apmt.2019.04.001>.
- [36] D.B. Miracle, O.N. Senkov, A critical review of high entropy alloys and related concepts, *Acta Mater.* (2017). <https://doi.org/10.1016/j.actamat.2016.08.081>.
- [37] R.S. Mishra, N. Kumar, M. Komarasamy, Lattice strain framework for plastic deformation in complex concentrated alloys including high entropy alloys, *Mater. Sci. Technol.* 31 (2015) 1259–1263. <https://doi.org/10.1179/1743284715Y.0000000050>.
- [38] J.W. Yeh, S.K. Chen, J.Y. Gan, S.J. Lin, T.S. Chin, T.T. Shun, C.H. Tsau, S.Y. Chang, Formation of simple crystal structures in Cu-Co-Ni-Cr-Al-Fe-Ti-V alloys with multiprincipal metallic elements, *Metall. Mater. Trans. A Phys. Metall. Mater. Sci.* 35 A (2004) 2533–2536. <https://doi.org/10.1007/s11661-006-0234-4>.
- [39] M.R. Chen, S.J. Lin, J.W. Yeh, S.K. Chen, Y.S. Huang, M.H. Chuang, Effect of vanadium addition on the microstructure, hardness, and wear resistance of Al0.5CoCrCuFeNi high-entropy alloy, *Metall. Mater. Trans. A Phys. Metall. Mater. Sci.* 37 (2006) 1363–1369. <https://doi.org/10.1007/s11661-006-0081-3>.
- [40] M.H. Tsai, K.Y. Tsai, C.W. Tsai, C. Lee, C.C. Juan, J.W. Yeh, Criterion for sigma phase formation in Cr- and V-Containing high-entropy alloys, *Mater. Res. Lett.* 1 (2013) 207–212. <https://doi.org/10.1080/21663831.2013.831382>.
- [41] Y. Dong, K. Zhou, Y. Lu, X. Gao, T. Wang, T. Li, Effect of vanadium addition on the microstructure and properties of AlCoCrFeNi high entropy alloy, *Mater. Des.* 57 (2014) 67–72. <https://doi.org/10.1016/j.matdes.2013.12.048>.

- [42] B.S. Li, Y.P. Wang, M.X. Ren, C. Yang, H.Z. Fu, Effects of Mn, Ti and V on the microstructure and properties of AlCrFeCoNiCu high entropy alloy, *Mater. Sci. Eng. A.* 498 (2008) 482–486. <https://doi.org/10.1016/j.msea.2008.08.025>.
- [43] G. Qin, S. Wang, R. Chen, H. Zheng, L. Wang, Y. Su, J. Guo, H. Fu, Improvement of Microstructure and Mechanical Properties of CoCrCuFeNi High-Entropy Alloys By V Addition, *J. Mater. Eng. Perform.* 28 (2019) 1049–1056. <https://doi.org/10.1007/s11665-018-3837-1>.
- [44] P.J. Barron, A.W. Carruthers, J.W. Fellowes, N.G. Jones, H. Dawson, E.J. Pickering, Towards V-based high-entropy alloys for nuclear fusion applications, *Scr. Mater.* 176 (2020) 12–16. <https://doi.org/10.1016/j.scriptamat.2019.09.028>.
- [45] S.S. Nene, M. Frank, K. Liu, S. Sinha, R.S. Mishra, B.A. McWilliams, K.C. Cho, Corrosion-resistant high entropy alloy with high strength and ductility, *Scr. Mater.* 166 (2019) 168–172. <https://doi.org/10.1016/j.scriptamat.2019.03.028>.
- [46] T. Wang, S. Shukla, M. Komarasamy, K. Liu, R.S. Mishra, Towards heterogeneous Al x CoCrFeNi high entropy alloy via friction stir processing, *Mater. Lett.* 236 (2019) 472–475. <https://doi.org/10.1016/j.matlet.2018.10.161>.
- [47] S. Sinha, M. Komarasamy, S. Thapliyal, B. Gwalani, S. Shukla, K.A. Darling, R.S. Mishra, Immiscible nanostructured copper-aluminum-niobium alloy with excellent precipitation strengthening upon friction stir processing and aging, *Scr. Mater.* 164 (2019) 42–47. <https://doi.org/10.1016/j.scriptamat.2019.01.038>.
- [48] E. Polatidis, J. Čapek, A. Arabi-Hashemi, C. Leinenbach, M. Strobl, High ductility and transformation-induced-plasticity in metastable stainless steel processed by selective laser melting with low power, *Scr. Mater.* 176 (2020) 53–57. <https://doi.org/10.1016/j.scriptamat.2019.09.035>.
- [49] A.J. Bogers, W.G. Burgers, Partial dislocations on the {110} planes in the B.C.C. lattice and the transition of the F.C.C. into the B.C.C. lattice, *Acta Metall.* 12 (1964) 255–261. [https://doi.org/10.1016/0001-6160\(64\)90194-4](https://doi.org/10.1016/0001-6160(64)90194-4).
- [50] J.A. Venables, The martensite transformation in stainless steel, *Philos. Mag.* 7 (1962) 35–44. <https://doi.org/10.1080/14786436208201856>.
- [51] G. Kurdjumow, G. Sachs, Über den Mechanismus der Stahlhärtung, *Zeitschrift Für Phys.* 64 (1930) 325–343. <https://doi.org/10.1007/BF01397346>.
- [52] P. Behjati, A. Najafizadeh, Role of chemical driving force in martensitic transformations of high-purity Fe-Cr-Ni alloys, in: *Metall. Mater. Trans. A Phys. Metall. Mater. Sci.*, Springer, 2011: pp. 3752–3760. <https://doi.org/10.1007/s11661-011-0769-x>.
- [53] R. Lagneborgj, The martensite transformation in 18% Cr-8% Ni steels, *Acta Metall.* 12 (1964) 823–843. [https://doi.org/10.1016/0001-6160\(64\)90176-2](https://doi.org/10.1016/0001-6160(64)90176-2).
- [54] M. Zecevic, M. V. Upadhyay, E. Polatidis, T. Panzner, H. Van Swygenhoven, M. Knezevic, A crystallographic extension to the Olson-Cohen model for predicting strain path dependence of martensitic transformation, *Acta Mater.* 166 (2019) 386–401. <https://doi.org/10.1016/j.actamat.2018.12.060>.
- [55] E. Polatidis, W.N. Hsu, M. Šmíd, T. Panzner, S. Chakrabarty, P. Pant, H. Van

Swygenhoven, Suppressed martensitic transformation under biaxial loading in low stacking fault energy metastable austenitic steels, *Scr. Mater.* 147 (2018) 27–32. <https://doi.org/10.1016/j.scriptamat.2017.12.026>.

- [56] T.S. Byun, On the stress dependence of partial dislocation separation and deformation microstructure in austenitic stainless steels, *Acta Mater.* 51 (2003) 3063–3071. [https://doi.org/10.1016/S1359-6454\(03\)00117-4](https://doi.org/10.1016/S1359-6454(03)00117-4).

## Acknowledgments

The authors thank the Center of Agile and Adaptive Additive Manufacturing (CAAAM) and Materials Research Facility (MRF) for access to the microscopy facilities. The authors also thank Mr. Michael Toll for preparation of the samples for testing and microscopy.

## Data availability

The raw/processed data required to reproduce these findings cannot be shared at this time, as the data are also part of other ongoing studies.